



Full Length Article

Anisotropic microstructure evolution of an AZ31B magnesium alloy subjected to dry sliding and its effects on friction and wear performance

Bo Mao, Xing Zhang, Pradeep L. Menezes, Yiliang Liao*

Department of Mechanical Engineering, University of Nevada, Reno, Reno, NV 89557 USA



ARTICLE INFO

Keywords:

Magnesium alloys
Microstructure evolution
Friction
Wear
Anisotropy

ABSTRACT

Due to their hexagonal closed-packed (HCP) crystal structure, magnesium (Mg) and its alloys typically exhibit strong plastic anisotropy which gives rise to their orientation-dependent mechanical properties. Tribological performance in terms of friction and wear is of critical importance to manufacturing and applications of Mg alloys, particularly for components subjected to sliding motion. However, anisotropic microstructure evolution of Mg alloy and its effects on friction and wear properties have rarely been investigated. In this study, the orientation-dependent microstructure behaviors of an AZ31B Mg alloy during dry sliding were investigated. The coefficient of friction (COF) and wear rate of worn surfaces were analyzed and compared. The results indicated pronounced anisotropic friction and wear behaviors. The mechanism responsible for the anisotropic tribological behaviors was discussed.

1. Introduction

As lightest structural metallic materials, magnesium (Mg) and its alloys have a density of 1.74 g/cm^3 , which is only 22% and 64% as those of steels (7.87 g/cm^3) and aluminum alloys (2.7 g/cm^3), respectively [1]. Mg alloys possess some excellent physical and mechanical properties such as high strength-to-weight ratio [2], good recyclability [3], and desirable bio-compatibility [4]. All of these characteristics make Mg alloys promising for applications in aircraft [5], automotive [6], bio-implants [7], and electronic devices [8].

Mg alloys have a hexagonal closed-packed (HCP) crystal structure with low symmetry, which endows them unique plastic behaviors as compared with commonly used metallic materials with a cubic crystal structure [9]. Among the limited slip systems of Mg crystal, the critical resolved shear stress (CRSS) for $\langle a \rangle$ basal slip is much lower than $\langle c + a \rangle$ slip [10]. Commercially used Mg alloys are mainly manufactured by hot extrusion or rolling due to their superior mechanical properties to the casting counterparts [11]. However, wrought Mg alloys typically exhibit a strong basal texture in which most of grains are oriented such that their basal planes are perpendicular to a specific direction [12–14]. Therefore, Mg alloys typically exhibit orientation-dependent mechanical properties, as evidenced by their anisotropic behaviors in tension [15–17], compression [18,19], and fatigue endurance [20,21]. For instance, Park et al. [19] reported that the stress level of an extruded AZ31 Mg alloy during monotonic compression tests along normal direction (ND) was 1.7 times higher than that along rolling direction (RD) at a strain of 0.04. Suh et al. [22] showed the yield strength of an Mg–

Zn–Ga alloy during monotonic tensile tests along RD was 35% higher than that along transverse direction (TD). Xiong and Jiang [23] showed that an rolled AZ80 Mg alloy exhibited the lowest fatigue life as the cyclic loading was applied along ND, as compared to tested along RD and TD.

Tribological performance in terms of friction and wear is of critical importance to manufacturing and applications of Mg alloys, particularly for components subjected to sliding motion such as bearings, pistons, and valves [24]. Fundamentally speaking, friction and wear behaviors are results of materials' responses to localized deformation [25,26]. Therefore, it is expected that tribological behaviors of Mg alloys have an inherent relationship with their plastic anisotropy. However, despite extensive research efforts in understanding tribo-performance of Mg alloys as affected by microstructure features of grain size [27,28], twins [29], and precipitates [30], anisotropic tribological properties of Mg alloys have rarely been investigated.

In this study, the orientation-dependent microstructure evolutions of an AZ31B Mg alloy subjected to dry sliding were investigated. Rolled AZ31B Mg alloys were selected as the experimental materials as they are among the most commonly used wrought Mg alloys for their ease of processing and adequate mechanical properties [4]. The friction and wear performance as affected by microstructural evolution during different sliding cases were studied. The coefficient of friction (COF) and wear rate of worn surfaces were analyzed and compared. The results indicated pronounced orientation-dependent friction and wear behaviors. The mechanism responsible for the anisotropic tribological behaviors was proposed and discussed.

* Corresponding author.

E-mail address: yliao@unr.edu (Y. Liao).

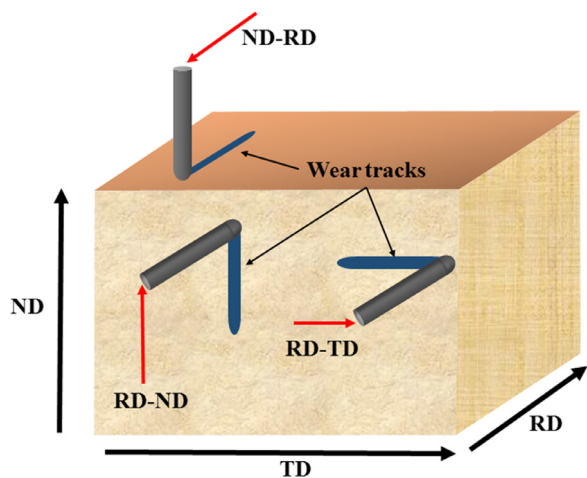


Fig. 1. A schematic illustration of the pin-on-plate tests and three sliding cases.

2. Experiments

2.1. Materials

The Mg alloy used in this study was a hot-rolled AZ31B Mg alloy block (Al-3.0%, Zn-1.0%, Mg-balance, in wt%) purchased from Metal-mart.com. Cubic samples with a width of 1 in. were cut from the block with three orthotropic sections perpendicular to RD, TD, and ND. All samples were homogenized in a vacuum furnace at 200 °C for 1 h to remove possible artifacts (such as near surface dislocations and residual stress) induced by machining [31]. Noted that the strong basal texture and anisotropy of rolled Mg alloys are not changed during static annealing process [32,33]. Sample surfaces perpendicular to the ND and RD were grinded by silicon carbide papers followed by polishing with diamond suspensions with particle sizes of 3 and 1 μm.

2.2. Dry sliding testing

Tribological properties of Mg alloy samples were tested using an Rtec Multi-function tribometer 5000 with a pin-on-plate configuration.

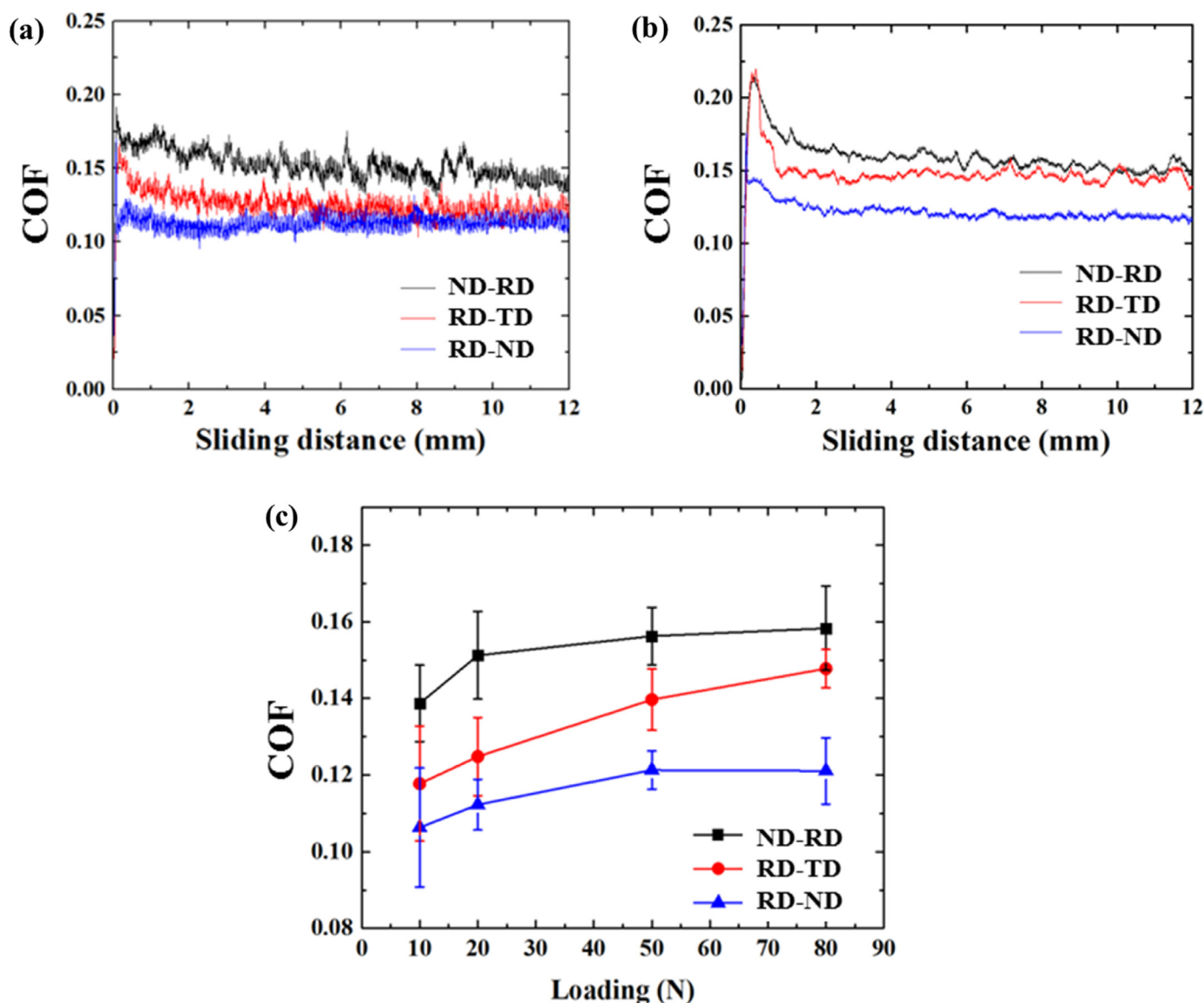


Fig. 2. (a) and (b) Anisotropic COFs of Mg alloy samples in three sliding cases with a normal load of 20 N and 80 N, respectively. (c) Orientation-dependent COFs as affected by normal loads.

Aluminum alloy 6061-T6 (AA6061) was chosen to make cylindrical pins with a hemispherical tip (a radius of 3.2 mm). The hardness of the pin material was around 110 VHN (Vickers Hardness Number). The pins were slid on different surfaces of Mg alloy samples along different directions. As shown in Fig. 1, three sliding cases which are marked as ND-RD, RD-TD, and RD-ND, representing sliding along RD on the surface perpendicular to ND, sliding along TD on the surface perpendicular to RD, and sliding along ND on the surface perpendicular to RD, respectively, were investigated. Noted that although there are six sliding cases of ND-RD, ND-TD, RD-ND, RD-TD, TD-ND, and TD-RD, only three of them need to be investigated due to the crystallographic texture symmetry Mg alloy block. Applied normal loads of 10, 20, 50, and 80 N were used in each sliding case whereas the sliding speed was fixed to be 2 mm/s. All testing works were carried out in a dry condition under ambient environment. Dry sliding test was conducted since it was the first and simplest step towards understanding of complicated tribo-systems. The COFs in three sliding cases, μ_{ND-RD} , μ_{RD-TD} , and μ_{RD-ND} in each test were recorded.

2.3. Characterization

The worn surface morphologies of samples after sliding tests were characterized using a Leica DM2700 optical microscope (OM), scanning electron microscope (SEM, JEOL-2100) equipped with energy dispersive X-ray spectroscopy (EDS) source, and three-dimensional (3D) optical profilometer (Rtec Instruments) with a spatial resolution of 0.25 μm . To reveal the microstructure evolution during sliding process, the surface and cross-section of the samples were vibrationally polished with

a 0.06 μm diamond suspension for 1 h and then etched by an acetic picral solution (10 ml acetic acid + 4.2 g picric acid + 10 ml distilled water + 70 ml ethanol) for OM and electron backscattered diffraction (EBSD) analysis. The EBSD data acquisition was performed with Channel 5 software on the patterned area with a step size of 0.5 μm .

3. Results

3.1. Anisotropic friction behavior

Fig. 2(a) and (b) shows anisotropic COFs of Mg alloy samples in three sliding cases with a normal load of 20 N and 80 N, respectively. It can be seen that the COF becomes stable after a sliding distance shorter than 2 mm for all sliding cases. In addition, the recorded COFs during sliding tests under a load of 80 N exhibit less fluctuation as compared to those under a load of 20 N due to the decrease of stick-slip amplitude [34]. More importantly, the mean values of COFs exhibit an order as, $\mu_{ND-RD} > \mu_{RD-TD} > \mu_{RD-ND}$, regardless of normal load. Fig. 2(c) shows orientation-dependent COFs as affected by normal loads. It is observed that the COF increases with the increase of normal load for all three sliding cases. For instance, during the RD-TD sliding test, the COF increases by 16% from 0.116 to 0.135 as the normal load increases from 10 to 50 N, and reaches 0.145 at a normal load of 80 N. Moreover, given a fixed normal load, the COF of RD-TD case is higher than that of RD-ND case while lower than that of ND-RD case. For example, given an applied load of 50 N, the average values of COFs are 0.115, 0.135, and 0.155 for RD-ND, RD-TD, and ND-RD cases, respectively.

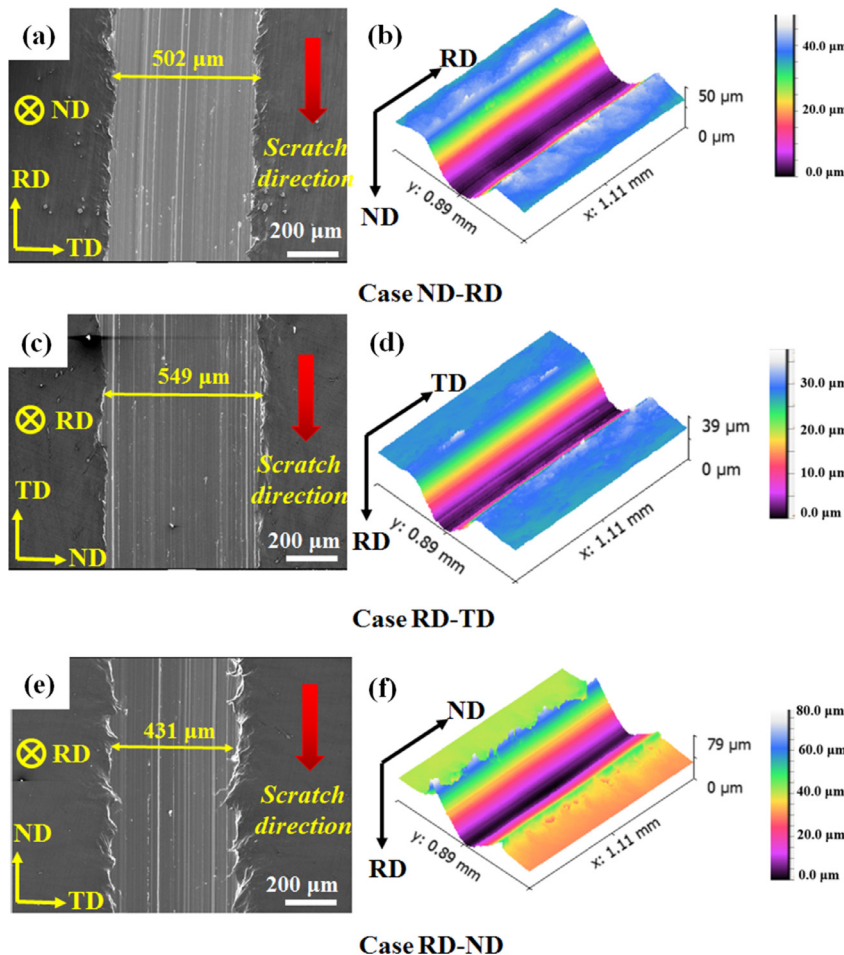


Fig. 3. SEM and 3D surface profile images of worn surfaces subjected to a sliding load of 80 N, the sliding case of: (a) and (b) ND-RD; (c) and (d) RD-TD; and (e) and (f) RD-ND.

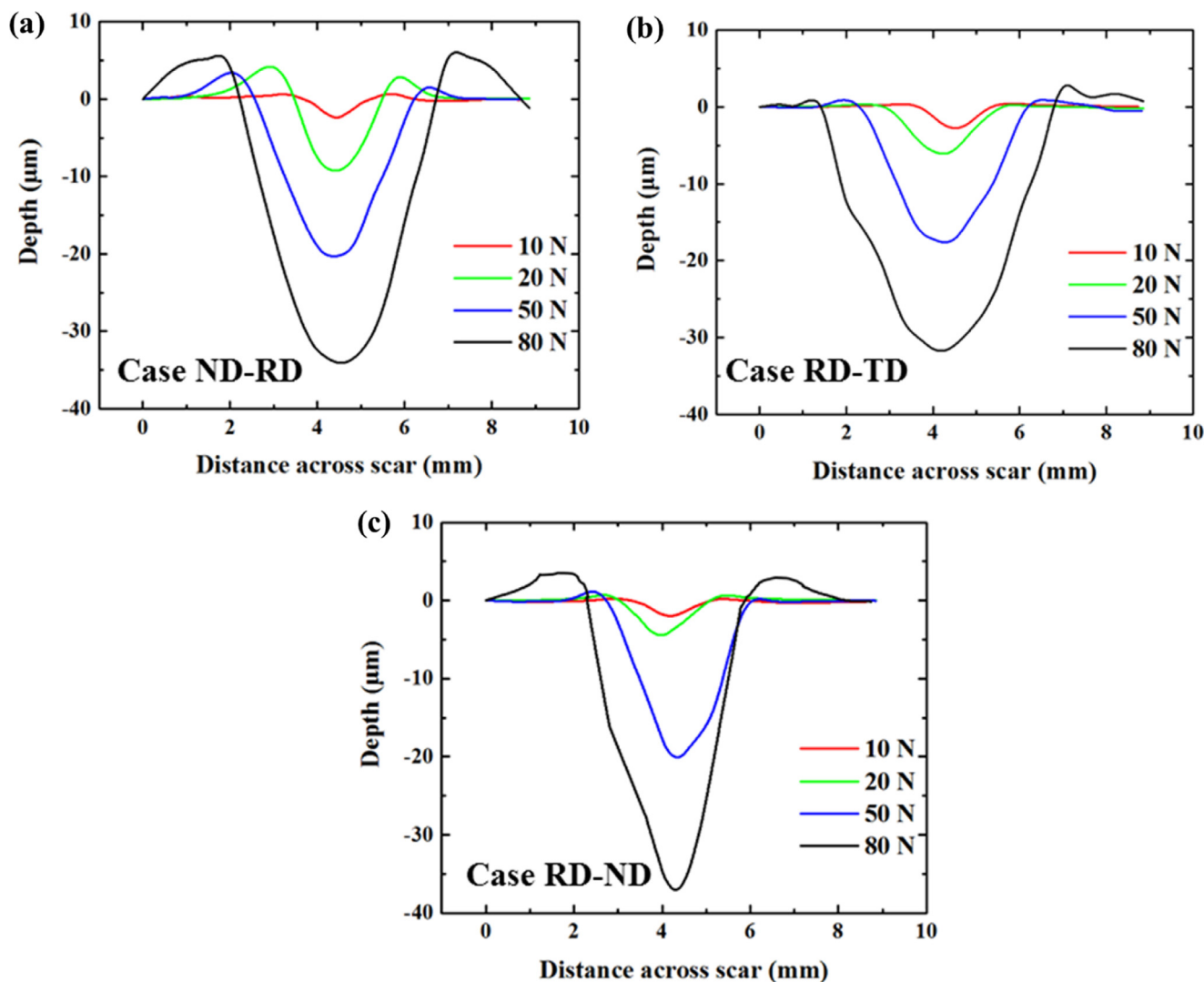


Fig. 4. Cross-sectional profiles of worm surfaces as affected by sliding load in three sliding cases: (a) ND-RD, (b) RD-TD, and (c) RD-ND.

3.2. Anisotropic wear behavior

Fig. 3 shows SEM and 3D profile images of the worn surfaces in three sliding cases under an applied load of 80 N. As observed in the SEM images (Fig. 3(a), (c), and (e)), the widths of wear tracks are orientation-dependent, which are 431, 502, 549 μm for the cases of RD-ND, ND-RD, and RD-TD, respectively. As observed in the 3D profile images (Fig. 3(b), (d), and (f)), the material is displaced to the edges of the wear tracks after sliding tests due to the plastic deformation. Micro-grooves are identified on the wear tracks due to the plowing effect. As the harder Al pin plow on the softer Mg alloy substrate, microgrooves are formed via plastic deformation or fragmentation [35]. The height of the wear track edge in the RD-TD case is considerably lower than those in the other two cases. To be specific, the height of displaced material on wear track edges is around 0.5 μm in the RD-TD case, as compared to those of 5 μm in the ND-RD and RD-ND cases.

Fig. 4 presents the two-dimensional (2D) cross-sectional profiles of wear tracks in three sliding cases under various loads. It is found that the wear track depth increases with an increase in sliding load. For instance, the wear track depth increases from 4.2 μm under the load of 10 N to 35.4 μm under the load of 80 N in the ND-RD case. Moreover, the anisotropic wear behavior becomes significant under a high sliding load. Specifically, the RD-ND case exhibits the highest wear track depth, while the RD-TD case has the lowest one. For instance, with a

load of 80 N, the depths of wear track are 32.2, 35.4, 38.7 μm for RD-TD, ND-RD and RD-ND sliding cases, respectively. However, the wear tracks are narrowest for the sliding case of RD-ND (Fig. 3). In addition, the orientation-dependent height of the wear track edges observed in Fig. 3 is confirmed in Fig. 4. The experimental results in Figs. 3 and 4 demonstrated the anisotropic wear behavior of Mg alloys.

The 3D surface profiles of wear track front of worn surfaces subjected to a sliding load of 80 N were examined as shown in Fig. 5. It can be seen that the surface pile-up morphologies at the wear track front are also orientation-dependent. The 2-D profiles along the dash lines in Fig. 5(a)–(c) are shown in Fig. 5(d). By comparing the heights of the surface piles-up morphologies at the wear track front, it is found the RD-TD case exhibits the largest value of 15.2 μm , while the RD-ND case exhibits the lowest value of 5.4 μm . Noted that wear tests in this work were conducted at the macroscale. Based on the scale of interests (from nano to macro), various wear testing approaches have been developed [36–39]. The complexity and multi-scale nature of interactions at contact interfaces can be revealed by these approaches. The anisotropic tribo-performance of Mg alloys at the micro- and/or nano-scale will be investigated in another effort.

In order to understand the dominant wear mechanism, EDS analysis was performed on sample surfaces after sliding tests, as shown in Fig. 6. There is no significant difference in chemical compositions of worn surface between the three sliding cases. The three worn surfaces

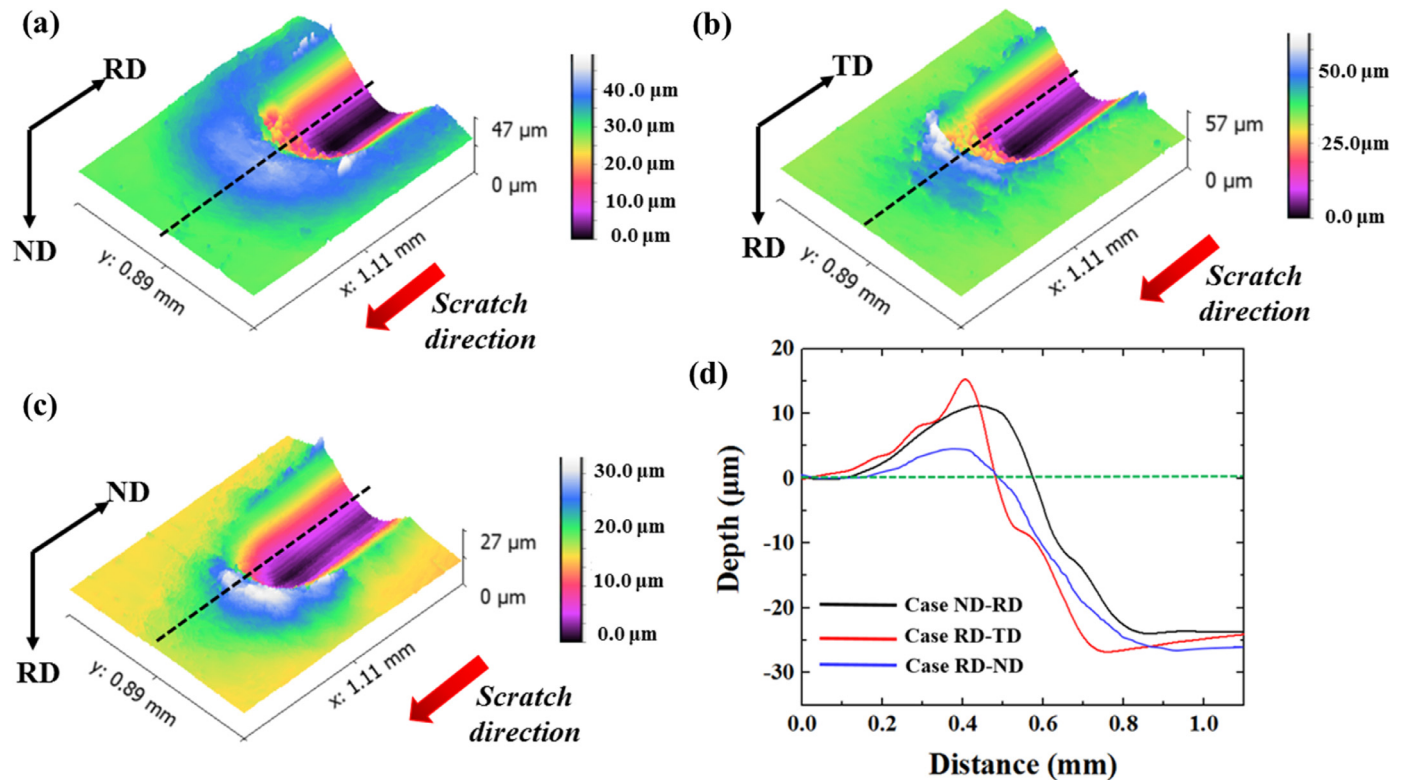


Fig. 5. 3D surface profiles of the front parts of worn surfaces subjected to a sliding load of 80 N, the sliding cases of: (a) ND-RD, (b) RD-TD, and (c) RD-ND. (d) 2D profiles of the front parts of worn surfaces.

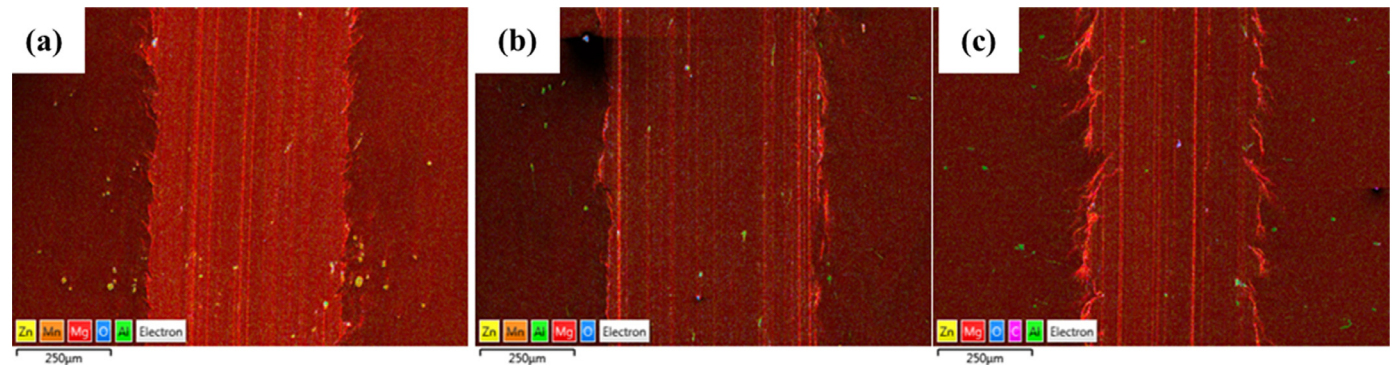


Fig. 6. EDS phase mapping analysis of wear tracks in three sliding cases under the load of 80N: (a) ND-RD, (b) RD-TD, and (c) RD-ND.

are mainly composed of Mg, while Al is barely observed. Some wear debris with chemical composition consisting of Mg and O are identified for three sliding cases. The SEM and EDS analysis of worn surfaces indicate that the dominant wear mechanism of Mg alloys in the current experiments is abrasion wear together with oxidation, which is consistent with previous studies [40,41].

4. Discussion

4.1. Surface hardness

To reveal the mechanism responsible for the anisotropic tribological behaviors of Mg alloys, Vickers hardness tests were carried out the surfaces perpendicular to ND and RD of Mg alloy samples. The hardness tests were conducted on a Wilson Hardness tester with a load of 0.5 kg and 10 s dwelling time. The results show that the average VHNS are 62.5 and 61.1 on the surfaces perpendicular to ND and RD, respec-

tively. The orientation-dependent surface hardness is negligible considering the experimental error. This finding was also reported in previous studies [42,43].

Surface hardness has been deemed to have a significant impact on the tribological behavior of metallic materials [44–46]. For instance, the well-known Archard's law postulated that the wear volume of a material during sliding is inversely proportional to its hardness [47], expressed as: $V = \frac{LkW}{H}$, where V is the wear volume, L is the sliding distance, W is the normal load, H is the hardness of the softer material in the contacting pair, and k is the wear coefficient. However, it can be seen that the anisotropic friction and wear behaviors of Mg alloys appear to be more complicated, which can be reflected by the different wear track morphologies but the same surface hardness on three sliding cases. Similar observations were reported by Hector et al. [38,39]. They ascribed the discrepancy to the scale effect originated from a number of reasons including change of dislocation density, material anisotropy, elastic and inelastic recovery [48].

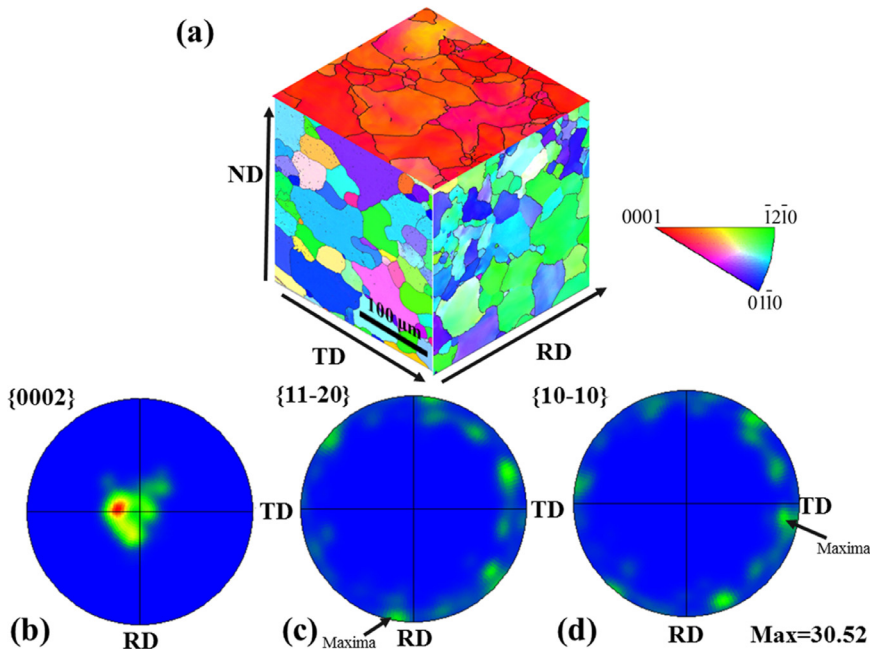


Fig. 7. Microstructure of the as-received AZ31B Mg alloy sample: (a) 3-D IPF map, the {0001} pole are corresponding to the ND, RD, and TD for the surface perpendicular to ND, RD, and TD. (b) {0002}, (c) {11-20}, and (d) {10-10} PF map of the surface perpendicular to ND.

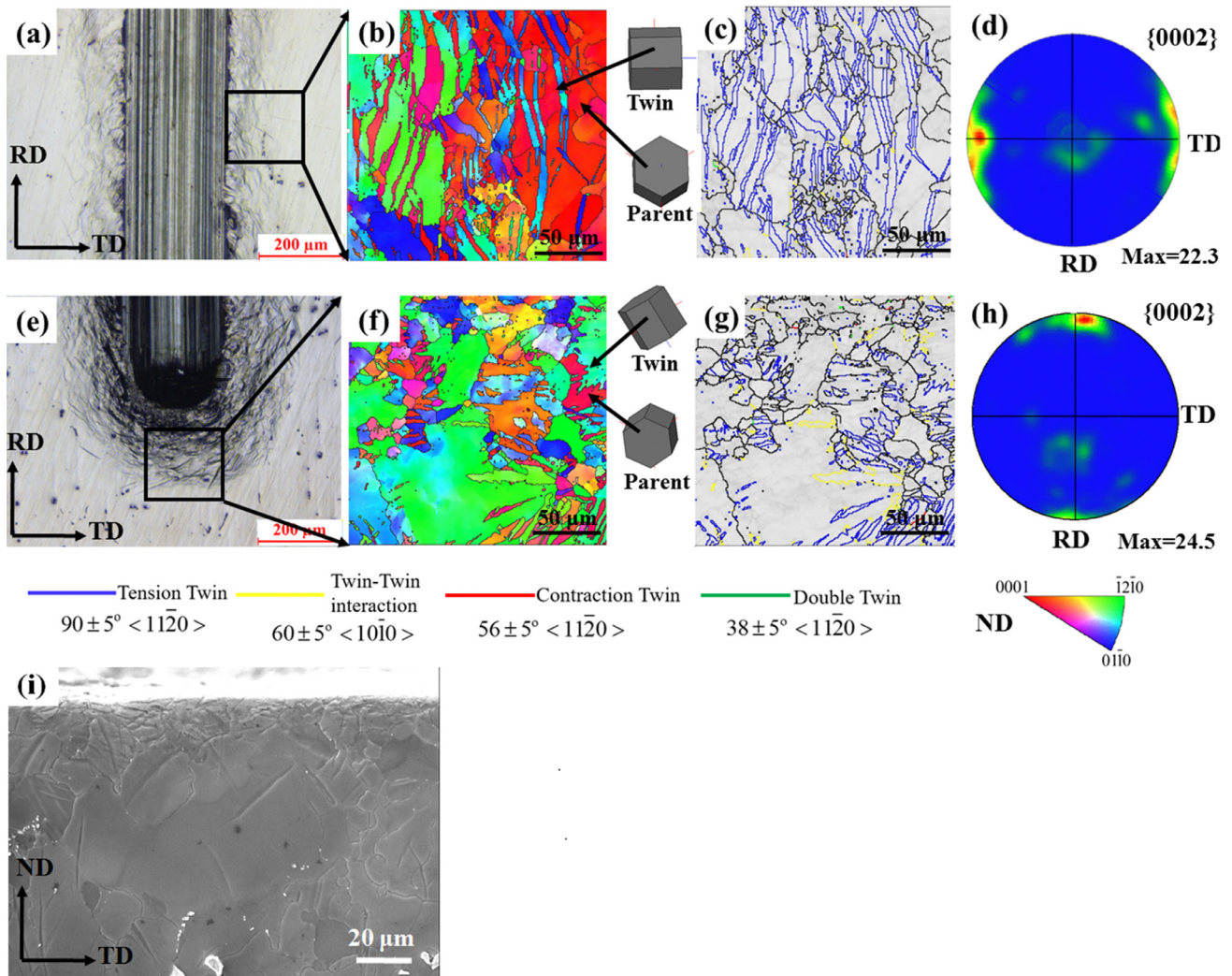


Fig. 8. Microstructure analysis of the worn surface of Mg alloy sample after sliding test (the case of ND-RD under the load of 20 N). Wear track edge: (a) OM image, (b) IPF map, (c) image quality map, and (e) {0002} PF map. Wear track front: (e) OM image, (f) IPF map, (g) image quality map, and (h) {0002} PF map. (i) SEM image of the cross-sectional microstructure beneath the wear track.

4.2. Anisotropic microstructural evolution

Besides the surface hardness, the microstructure evolution during sliding plays another key role on determining tribological properties. To study the microstructure evolution of Mg alloys during sliding, EBSD characterization was performed on the annealed Mg alloy samples before the sliding tests. Fig. 7(a) shows the 3D inverse pole figure (IPF) maps which were constructed from three different surfaces. It can be seen that the material has an equiaxed, twin-free grain structure with an average grain size of around 25 μm . The $\{0002\}$ pole figure (PF) of the surface perpendicular to ND shows the material has a very strong basal texture, in which most of the c -axis of the HCP crystals are parallel to ND (Fig. 7(b)). Moreover, the $\{10\bar{1}0\}$ and $\{11\bar{2}0\}$ PF show that most of the stereographic projection of $\{11\bar{2}0\}$ and $\{10\bar{1}0\}$ axis exhibit a spherical distribution. However, the majority of $\{11\bar{2}0\}$ directions are parallel to the RD (Fig. 7(c)) and $\{10\bar{1}0\}$ directions are parallel to the TD (Fig. 7(d)).

The microstructure of Mg alloy samples after sliding tests was characterized using EBSD and OM. The OM images in Fig. 8(a) and (e) show the wear track and its front part in the sliding case of ND-RD under the load of 20 N, respectively. It can be seen that the surface pile-up

regions, corresponding to the edge and front parts of the wear track as observed in Figs. 3(a) and 5(a), are distributed along the scratch direction and around the front of wear track. EBSD analysis of wear track edges was conducted, as shown in Fig. 8(b)–(d). From the IPF map in Fig. 8(b), it can be seen that a large amount of twin lamellas are formed in the parent grains. The crystallographic orientation of one twin variant and parent grain shows the misorientation between them is almost 90° , indicating that the twins are formed by $\{10\bar{1}2\}\{10\bar{1}\bar{1}\}$ extension twinning mode [49]. The formation of $\{10\bar{1}2\}$ twins on the wear track edges is attributed to the compressive stress field in this area. Moreover, the twin density decreases with the increase of distance from the wear track center, indicating a gradient compressive strain field since the strain accommodated by extension twinning is proportionally to twin volume fraction [50–52]. Different types of grain boundaries are highlighted with different colors in the image quality map in Fig. 8(c). It can be seen that $\{10\bar{1}2\}$ extension twins, which are characterized by the twin boundaries of $86.3 \pm 5^\circ \langle 11\bar{2}0 \rangle$, profusely exist in this area. In addition, twin–twin interactions, which are characterized by the yellow boundaries and which resulted from the impingement of different $\{10\bar{1}2\}$ twin variants, can be identified [53,54]. The PF map in Fig. 8(d) (as compared to Fig. 7(b)) shows the crystallographic texture of the microstructure on

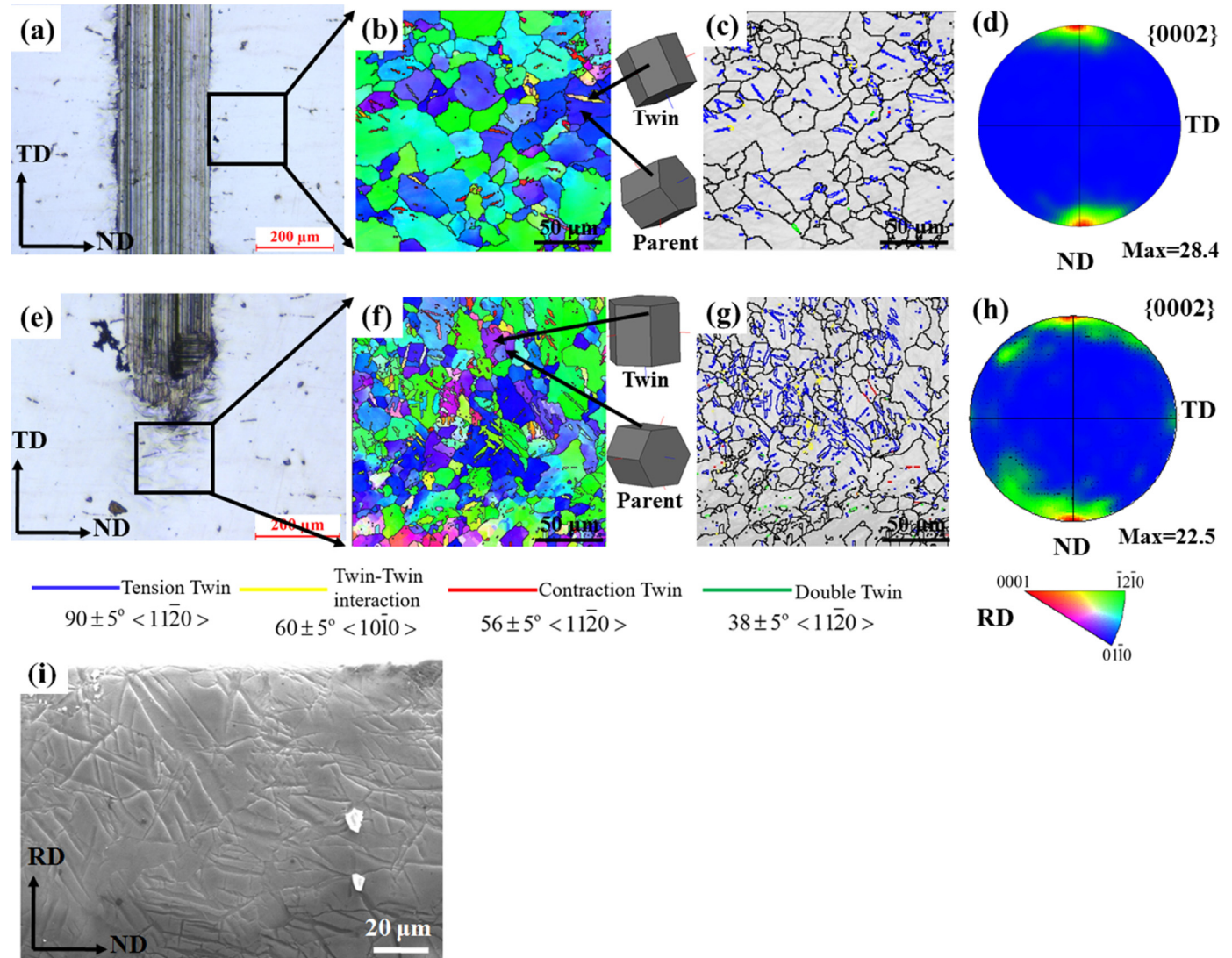


Fig. 9. Microstructure analysis of the worn surface of Mg alloy sample after sliding test (the case of RD-TD under the load of 20 N). Wear track edge: (a) OM image, (b) IPF map, (c) image quality map, and (e) $\{0002\}$ PF map. Wear track front: (e) OM image, (f) IPF map, (g) image quality map, and (h) $\{0002\}$ PF map. (i) SEM image of the cross-sectional microstructure beneath the wear track.

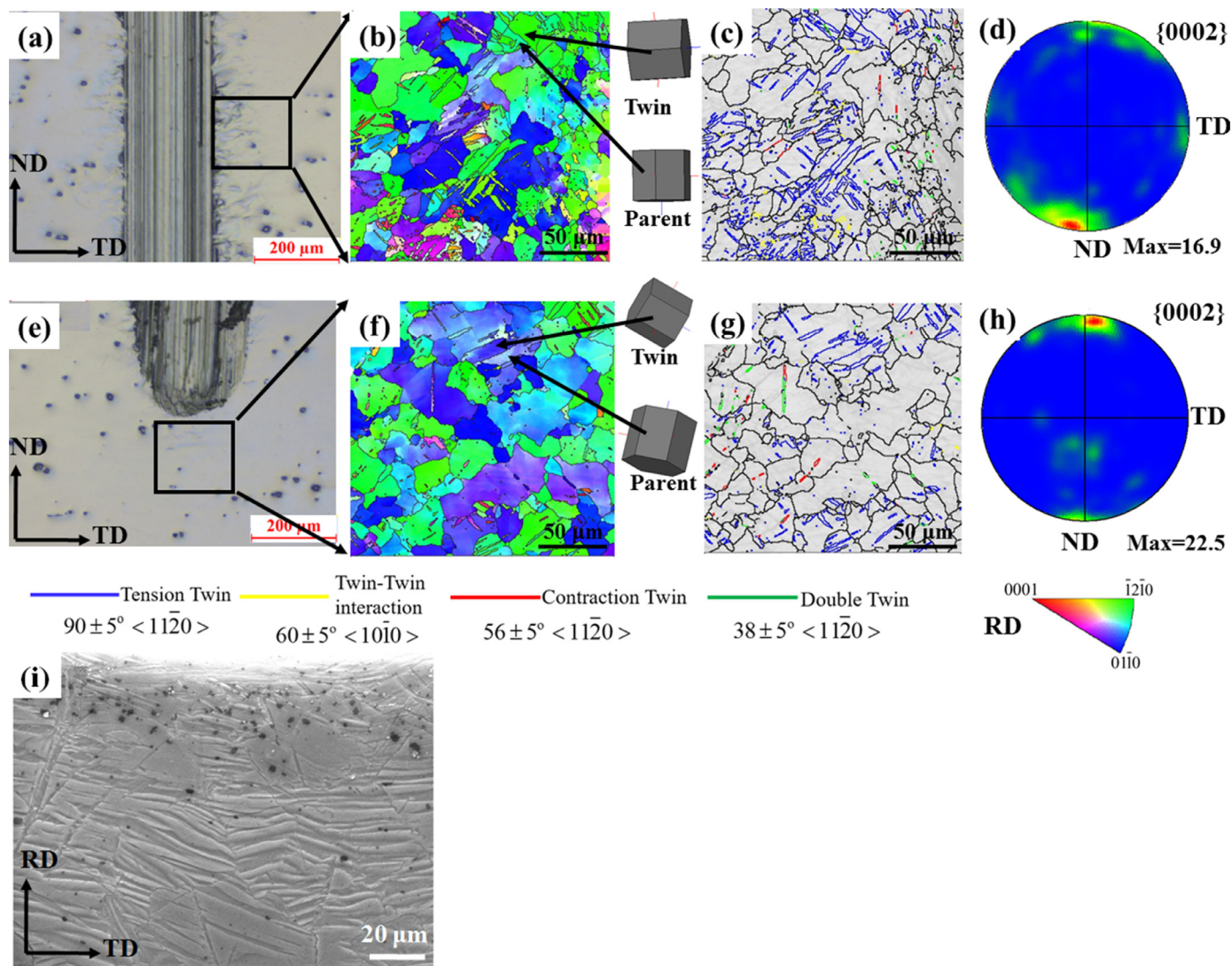


Fig. 10. Microstructure analysis of the worn surface of Mg alloy sample after sliding test (the case of RD-ND under the load of 20 N). Wear track edge: (a) OM image, (b) IPF map, (c) image quality map, and (e) $\{0002\}$ PF map. Wear track front: (e) OM image, (f) IPF map, (g) image quality map, and (h) $\{0002\}$ PF map. (i) SEM image of the cross-sectional microstructure beneath the wear track.

wear track edges is dramatically changed during sliding to accommodate the plastic strain induced by plowing. EBSD analysis of the front part of the wear track is shown in Fig. 8(f)–(h). The IPF map in Fig. 8(f) and image quality map in Fig. 8(g) indicate that the grains are almost fully twinned. The crystallographic orientation analysis in Fig. 8(f) and the PF map in Fig. 8(h) show that the majority of the c -axis of the crystals in the deformed microstructure are rotated to the RD. The crystallographic texture difference between Fig. 8(d) and (h) is mainly attributed to the difference in twin variant selection under different stress states [55]. Such a twin distribution was also observed in our previous study, in which localized plastic deformation was applied on the surface perpendicular to ND [56]. Some refined grains with a grain size of around $5\ \mu\text{m}$ can be identified in Fig. 8(b) and (f). SEM image in Fig. 8(i) of the cross-sectional microstructure indicates that very few twins are generated beneath the wear track and most of the grains exhibit a twin-free microstructure.

Microstructural evolution analysis was also performed on the Mg alloy sample in the sliding case of RD-TD under the load of 20 N. OM image in Fig. 9(a) demonstrates the surface morphology on wear track edges is smoother than that in the case of ND-RD as shown in Fig. 8(a). This is consistent with 2D surface profiles of wear tracks in Fig. 4. EBSD analysis

was carried out on an area of wear track edges as shown in Fig. 9(b)–(d). From the IPF map and image quality map, it can be seen that several $\{10\bar{1}2\}$ twin lamellas are formed in the parent grains (Fig. 9(b)–(c)). However the twin density is much lower than that in the case of ND-RD as shown in Fig. 8(b)–(c). The PF map in Fig. 9(d) shows the crystallographic texture remains the basal texture, which is due to the limited amount of $\{10\bar{1}2\}$ twins. OM image of the front part of wear track in Fig. 9(e) shows some surface wrinkles are generated, which is consistent with the highest pile-up regions as shown in Fig. 5. EBSD analysis wear track front is shown in Fig. 9(f)–(h). It is found that several $\{10\bar{1}2\}$ twin lamellas are formed. The twin density is higher than that in Fig. 9(b) but lower than that in Fig. 8(f). SEM image of cross-sectional microstructure in Fig. 9(i) shows large amount of twins is generated beneath the wear track.

Microstructural evolution analysis was also performed on the Mg alloy sample in the sliding case of RD-ND. OM images of the edge and front part of wear track are shown in Fig. 10(a) and (e), respectively. As compared to the case of RD-TD (Fig. 9), the RD-ND case exhibits a rough wear track edge and a smooth wear track front, as also evidenced by Figs. 3 and 5. EBSD analysis reveals that the rough wear track edge in the case of RD-ND corresponds to microstructure with a high twin

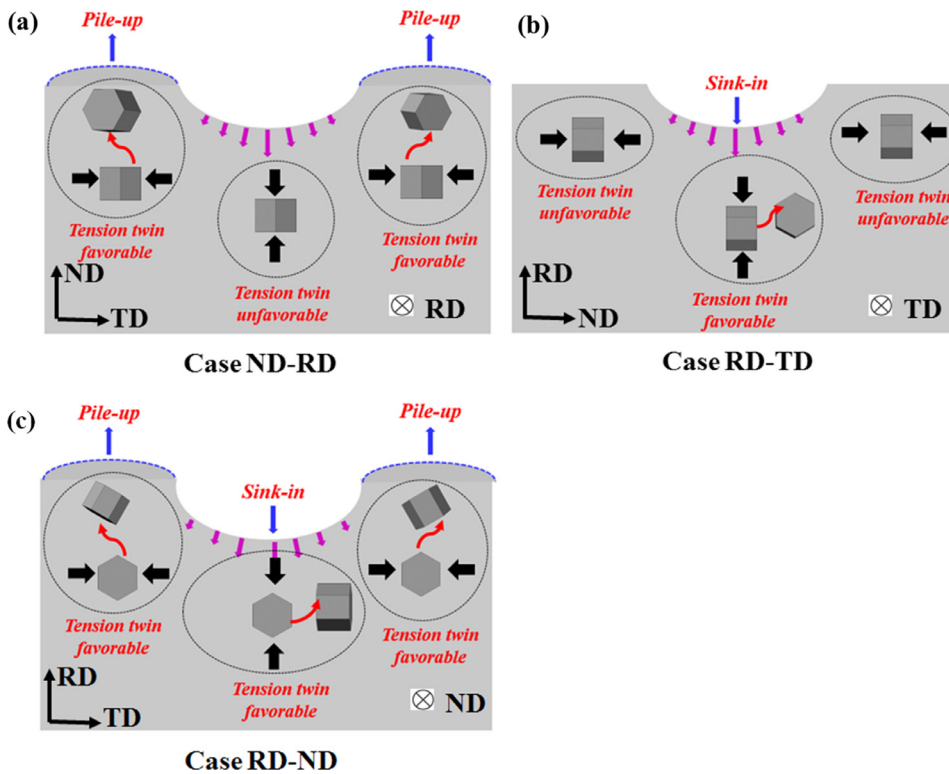


Fig. 11. Schematic illustrations of the cross-sectional crystallographic texture change of Mg alloy samples induced by sliding for cases of (a) ND-RD, (b) RD-TD, and (c) RD-ND.

density (Fig. 10(b)–(c)), whereas the smooth wear track front corresponds to microstructure with a low twin density (Fig. 10(f)–(g)). SEM image of cross-sectional microstructure in Fig. 10(i) shows a high density of twinning microstructure is generated beneath the wear track, which is similar to Fig. 9(i).

From the microstructure analysis in Figs. 8–10, it can be seen that Mg alloys experience different microstructure evolution in different sliding cases. The microstructure evolution is mainly attributed to the occurrence of $\{10\bar{1}2\}$ twinning, which has the lowest CRSS among all the plastic deformation modes of Mg [57]. The anisotropic microstructural response of Mg alloys subjected to sliding is responsible for the anisotropic tribological behavior.

4.3. The origin of tribological anisotropy

As the CRSS for $\{10\bar{1}2\}$ twinning mode in Mg alloys is low (~ 0.5 MPa) [58], it dominates the early plastic deformation stage of Mg alloys during the localized plastic deformation process, as in the case of sliding [59,60]. The lattice rotation associated with the formation of $\{10\bar{1}2\}$ twins leads to the change of crystallographic texture of Mg alloys [61], resulting in the anisotropic plastic deformation behavior. Therefore, particular focus should be put on the twinning-induced surface texture change to address the anisotropic tribological behavior of Mg alloys under dry sliding contact.

The stress state as well as twinning modes in three different sliding cases are presented in Fig. 11(a)–(c). For the ease of our discussion, an ideal texture model is proposed, in which the c axis of all HCP crystals are defined to be parallel to ND, $\{10\bar{1}0\}$ directions are parallel to the TD, and $\{11\bar{2}0\}$ directions are parallel to the RD, based on the initial microstructure in Fig. 7. Such crystallographic texture is also observed in most of the rolled Mg alloys [62,63]. As the normal load is performed along the ND, the grains underneath the indented surface experience compressive stress state which is tension twin unfavorable. Therefore few twins can be observed in Fig. 8(i). However, for the wear track edge area, $\{10\bar{1}2\}$ twinning mode is favorable since compressive stress are performed perpendicular to the ND (Fig. 11(a)). Since the activa-

tion of a specific twin variant is dependent on the stress state applied on the parent grain [64], the crystal orientation is rotated in a way in Fig. 11(a), as evidenced by the microstructure in Fig. 8(b) and (f). Moreover, $\{10\bar{1}2\}$ twinning has been proved to be responsible for the surface step formation [65], therefore the surface pile-up morphology on the edge of the wear tracks as shown in Figs. 3, 4, and 8 can be explained.

For the samples subjected to normal load along RD, the cross-sectional microstructure evolution model for the sliding cases of RD-TD and RD-ND are presented in Fig. 11(b) and (c), respectively. The compressive stress along RD promotes $\{10\bar{1}2\}$ twinning which takes place underneath the wear track, resulting in the surface sink-in phenomenon [42]. Therefore, the microstructure in Figs. 9(i) and 10(i) are characterized as large amount of twins. On the cross-section of microstructure in the sliding case of RD-TD, the stress state on wear track edges is unfavorable to $\{10\bar{1}2\}$ twinning. The plastic strain needs to be accommodated by compression twinning mode or $\langle c+a \rangle$ slip system, which requires much higher CRSS [66]. Therefore, no apparent surface pile-up morphology is observed in Fig. 4(b) and very few twins could be observed in Fig. 9(b)–(c). For the sliding case of RD-ND as shown in Fig. 11(c), the stress state on wear track edges favors $\{10\bar{1}2\}$ twinning (as shown in Fig. 10(b)–(c)) and results in a surface pile-up on the edge of the wear track (Fig. 3(f)). The combination of pile-up and sink-in leads to the result that the sliding case of RD-ND exhibits deepest wear track, as observed in Fig. 4.

Based on the above characterization and analysis, the mechanism responsible for the anisotropic tribological behavior of Mg alloys can be proposed. Fig. 12(a)–(c) schematically illustrate the side view and 3-D model of the contacting condition between tribo-pair of AA6061 pin and Mg alloy sample substrate. The crystallographic orientations of Mg grains at tribo-interfaces are also presented based on the microstructure observation and analysis in Figs. 7–10. For the sliding cases of ND-RD, the local plastic deformation at tribo-interfaces induces the crystallographic texture change, as presented by the two twin variants (Fig. 12(a)). In fact, since the grain size of the sample are much smaller than the width of wear track, the basal plane of the twin variants in front of the pin can be regarded as perpendicular to the sliding direction.

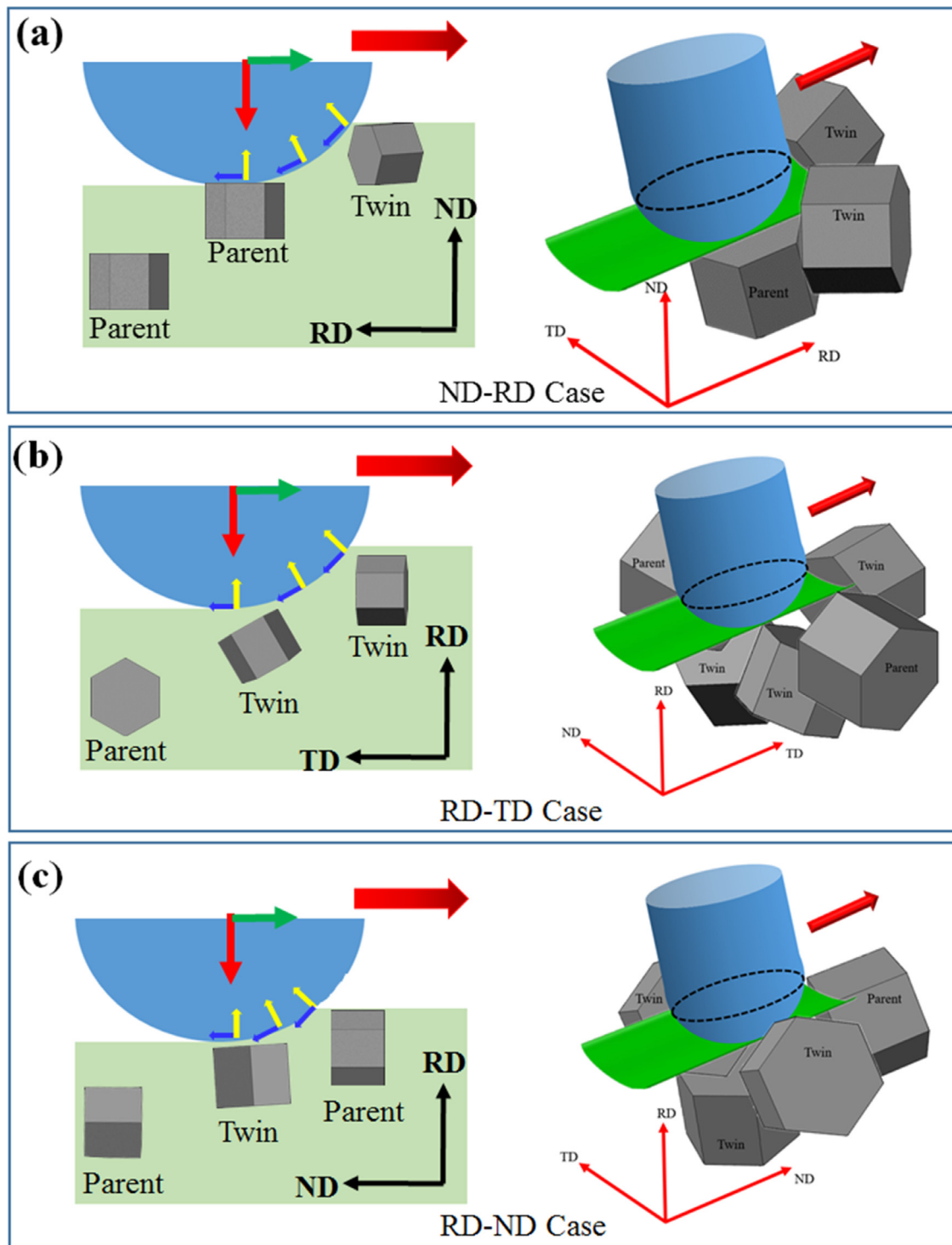


Fig. 12. Schematic of mechanism responsible for the anisotropic tribological properties of Mg alloys subjected to different sliding cases: (a) ND-RD, (b) RD-TD, and (c) RD-ND.

The accommodation of such shearing requires the activation of compression twinning and $\langle c+a \rangle$ slip mode, which have a much higher CRSS than those for basal slip and extension twins [67]. Moreover, the refined grains near the wear track (as shown in Fig. 8(f) also increases the shear strength due to the dynamic Hall–Petch effect [68–70]. Therefore, the sliding cases of ND-RD exhibits the highest COF. For the sliding case of RD-TD, continuous movement of pin also needs to shear the twin variants with a c axis parallel to the sliding direction (Fig. 10(b)). However, since the twin density in this case is much lower than that in the case

of ND-RD (Figs. 8(f) and 9(f)), less plowing force is needed to move the pin, resulting in a lower COF in the case of RD-TD as compared with the case of ND-RD. For the sliding case of RD-ND, deformation twinning mainly occurs at the edge of and beneath the wear tracks and the height of the surface pile-up at wear track front is much lower than those in the cases of ND-RD and RD-TD (Fig. 5(d)). Therefore, the required sliding force is lower due to the decrease of contacting area, leading to the lowest COF among all three sliding cases. Noted that the above analysis is based on a qualitative comparison rather than a quantitative estimation.

Therefore, modeling work will be carried out in our future research work to predict the friction force in different sliding directions.

5. Summary remarks and conclusions

In this study, the anisotropic tribological properties of an AZ31B Mg alloy were investigated by performing dry sliding tests along different sliding directions. The friction and wear performance as affected by microstructure behaviors were studied. The COF and wear rate of worn surfaces were compared. The following conclusions can be drawn:

- (1) Mg alloys exhibit prominent orientation-dependent friction behaviors under dry sliding condition. Among the three sliding cases in this study, the sliding case of ND-RD shows the highest COF (0.14–0.16) whereas the case of RD-ND has the lowest COF (0.10–0.12).
- (2) Mg alloys show prominent orientation-dependent wear behaviors under dry sliding condition. The RD-ND case has the deepest but narrowest wear tracks as compared to other two sliding cases.
- (3) The anisotropic tribo-performance is strongly associated with the orientation-related microstructure evolution. {10 $\bar{1}$ 2} tension twinning is found to have a significant impact on the friction and wear behaviors of Mg alloys since it determines the way of strain accommodation and crystallographic texture evolution during sliding tests.
- (4) A mechanism of orientation-dependent interfacial plastic deformation and crystallographic texture change is proposed to explain the anisotropic tribo-performance of Mg alloys under dry sliding condition.

Declaration of Competing Interest

The authors declare that they have no known competing financial interests or personal relationships that could have appeared to influence the work reported in this paper.

Acknowledgments

The authors appreciate the financial support by startup funding from the Department of Mechanical Engineering at the [University of Nevada, Reno](#).

References

- [1] T.M. Pollock, Weight loss with magnesium alloys, *Science* 328 (5981) (2010) 986–987.
- [2] G.S. Frankel, Magnesium alloys: ready for the road, *Nat. Mater.* 14 (12) (2015) 1189.
- [3] S. Wu, Z. Ji, T. Zhang, Microstructure and mechanical properties of AZ31B magnesium alloy recycled by solid-state process from different size chips, *J. Mater. Process. Technol.* 209 (12–13) (2009) 5319–5324.
- [4] C. Bettles, M. Gibson, Current wrought magnesium alloys: strengths and weaknesses, *JOM* 57 (5) (2005) 46–49.
- [5] I. Polmear, Magnesium alloys and applications, *Mater. Sci. Technol.* 10 (1) (1994) 1–16.
- [6] D. Mehta, S. Masood, W. Song, Investigation of wear properties of magnesium and aluminum alloys for automotive applications, *J. Mater. Process. Technol.* 155 (2004) 1526–1531.
- [7] M.P. Staiger, A.M. Pietak, J. Huadmai, G. Dias, Magnesium and its alloys as orthopedic biomaterials: a review, *Biomaterials* 27 (9) (2006) 1728–1734.
- [8] L.-Y. Chen, J.-Q. Xu, H. Choi, M. Pozuelo, X. Ma, S. Bhowmick, J.-M. Yang, S. Mathaudhu, X.-C. Li, Processing and properties of magnesium containing a dense uniform dispersion of nanoparticles, *Nature* 528 (7583) (2015) 539.
- [9] E. Burke, W. Hibbard, Plastic deformation of magnesium single crystals, *JOM* 4 (3) (1952) 295–303.
- [10] E. Kelley, W. Hosford, Plane-strain compression of magnesium and magnesium alloy crystals, *Trans. Met. Soc. AIME* 242 (1) (1968) 5–13.
- [11] E. Doege, K. Dröder, Sheet metal forming of magnesium wrought alloys—formability and process technology, *J. Mater. Process. Technol.* 115 (1) (2001) 14–19.
- [12] C.D. Barrett, A. Imandoust, A.L. Oppedal, K. Inal, M.A. Tschopp, H. El Kadiri, Effect of grain boundaries on texture formation during dynamic recrystallization of magnesium alloys, *Acta Mater.* 128 (2017) 270–283.
- [13] A. Rollett, S. Wright, *Typical Textures in Metals, Texture and Anisotropy: Preferred Orientations in Polycrystals and their Effect on Materials Properties*, Cambridge University Press, Edinburgh Building, Cambridge, CB 2 2 RU, UK, 1998, 1998, pp. 178–238.
- [14] U. Kocks, C. Tomé, H. Wenk, *Texture and Anisotropy*, Cambridge University Press, Cambridge, UK, 1998.
- [15] X. Zhang, Y. Cheng, Tensile anisotropy of AZ91 magnesium alloy by equal channel angular processing, *J. Alloys Compd.* 622 (2015) 1105–1109.
- [16] S.R. Agnew, Ö. Duygulu, Plastic anisotropy and the role of non-basal slip in magnesium alloy AZ31B, *Int. J. Plast.* 21 (6) (2005) 1161–1193.
- [17] A.R. Antoniswamy, E.M. Taleff, L.G. Hector Jr, J.T. Carter, Plastic deformation and ductility of magnesium AZ31B-H24 alloy sheet from 22 to 450C, *Mater. Sci. Eng.: A* 631 (2015) 1–9.
- [18] E. Yukutake, J. Kaneko, M. Sugamata, Anisotropy and non-uniformity in plastic behavior of AZ31 magnesium alloy plates, *Mater. Trans.* 44 (4) (2003) 452–457.
- [19] S.H. Park, S.-H. Kim, H. Yu, H.S. Kim, B.S. You, Anisotropic compressive behavior of extruded Mg alloy plates with different width–thickness ratios, *Mater. Sci. and Eng.: A* 675 (2016) 11–18.
- [20] S.H. Park, S.-G. Hong, W. Bang, C.S. Lee, Effect of anisotropy on the low-cycle fatigue behavior of rolled AZ31 magnesium alloy, *Mater. Sci. Eng.: A* 527 (3) (2010) 417–423.
- [21] K. Ahn, M.-H. Seo, Effect of anisotropy and differential work hardening on the failure prediction of AZ31B magnesium sheet at room temperature, *Int. J. Solids Struct.* 138 (2018) 181–192.
- [22] B.-C. Suh, J.H. Kim, J.H. Hwang, M.-S. Shim, N.J. Kim, Twinning-mediated formability in Mg alloys, *Sci. Rep.* 6 (2016) 22364.
- [23] Y. Xiong, Y. Jiang, Cyclic deformation and fatigue of rolled AZ80 magnesium alloy along different material orientations, *Mater. Sci. Eng. A* 677 (2016) 58–67.
- [24] P.J. Blau, M. Walukas, Sliding friction and wear of magnesium alloy AZ91D produced by two different methods, *Tribol. Int.* 33 (8) (2000) 573–579.
- [25] D. Rigney, J. Hirth, Plastic deformation and sliding friction of metals, *Wear* 53 (2) (1979) 345–370.
- [26] U. Olofsson, T. Telliskivi, Wear, plastic deformation and friction of two rail steels—a full-scale test and a laboratory study, *Wear* 254 (1–2) (2003) 80–93.
- [27] M. Shanthi, C. Lim, L. Lu, Effects of grain size on the wear of recycled AZ91 Mg, *Tribol. Int.* 40 (2) (2007) 335–338.
- [28] A. Amanov, O.V. Penkov, Y.-S. Pyun, D.-E. Kim, Effects of ultrasonic nanocrystalline surface modification on the tribological properties of AZ91D magnesium alloy, *Tribol. Int.* 54 (2012) 106–113.
- [29] B. Mao, A. Siddaiah, X. Zhang, B. Li, P.L. Menezes, Y. Liao, The influence of surface pre-twinning on the friction and wear performance of an AZ31B Mg alloy, *Appl. Surf. Sci.* 480 (2019) 998–1007.
- [30] A. Zafari, H. Ghasemi, R. Mahmudi, Effect of rare earth elements addition on the tribological behavior of AZ91D magnesium alloy at elevated temperatures, *Wear* 303 (1–2) (2013) 98–108.
- [31] B. Song, R. Xin, G. Chen, X. Zhang, Q. Liu, Improving tensile and compressive properties of magnesium alloy plates by pre-cold rolling, *Scr. Mater.* 66 (12) (2012) 1061–1064.
- [32] J.J. Bhattacharyya, S. Agnew, G. Muralidharan, Texture enhancement during grain growth of magnesium alloy AZ31B, *Acta Mater.* 86 (2015) 80–94.
- [33] Z. Zeng, Y. Zhu, S. Xu, M. Bian, C. Davies, N. Birbilis, J. Nie, Texture evolution during static recrystallization of cold-rolled magnesium alloys, *Acta Mater.* 105 (2016) 479–494.
- [34] C. Gao, D. Kuhlmann-Wilsdorf, D.D. Makel, The dynamic analysis of stick-slip motion, *Wear* 173 (1–2) (1994) 1–12.
- [35] K. Komvopoulos, N. Saka, N. Suh, Plowing friction in dry and lubricated metal sliding, *J. Tribol.* 108 (3) (1986) 301–312.
- [36] L. Peng, X. Lai, H.-J. Lee, J.-H. Song, J. Ni, Friction behavior modeling and analysis in micro/meso scale metal forming process, *Mater Des* 31 (4) (2010) 1953–1961.
- [37] B. Bhushan, J.N. Israelachvili, U. Landman, Nanotribology: friction, wear and lubrication at the atomic scale, *Nature* 374 (6523) (1995) 607.
- [38] L.G. Hector, S.R. Schmid, Simulation of asperity plowing in an atomic force microscope part I: experimental and theoretical methods, *Wear* 215 (1–2) (1998) 247–256.
- [39] S.R. Schmid, L.G. Hector, Simulation of asperity plowing in an atomic force microscope. Part II: plowing of aluminum alloys, *Wear* 215 (1–2) (1998) 257–266.
- [40] S. Wang, Z. Yang, Y. Zhao, M. Wei, Sliding wear characteristics of AZ91D alloy at ambient temperatures of 25–200 C, *Tribol. Lett.* 38 (1) (2010) 39–45.
- [41] J. An, Y. Zhang, X. Lv, Tribological characteristics of Mg–3Al–0.4 Si–0.1Zn alloy at elevated temperatures of 50–200 C, *Tribol. Lett.* 66 (1) (2018) 14.
- [42] R. Sánchez-Martín, M. Pérez-Prado, J. Segurado, J. Molina-Aldareguia, Effect of indentation size on the nucleation and propagation of tensile twinning in pure magnesium, *Acta Mater.* 93 (2015) 114–128.
- [43] B. Selvarajou, J.-H. Shin, T.K. Ha, I.-s. Choi, S.P. Joshi, H.N. Han, Orientation-dependent indentation response of magnesium single crystals: modeling and experiments, *Acta Mater.* 81 (2014) 358–376.
- [44] M. Mokhtar, The effect of hardness on the frictional behaviour of metals, *Wear* 78 (3) (1982) 297–304.
- [45] J. Reid, J. Schey, The effect of surface hardness on friction, *Wear* 118 (1) (1987) 113–125.
- [46] B. Mao, A. Siddaiah, P.L. Menezes, Y. Liao, Surface texturing by indirect laser shock surface patterning for manipulated friction coefficient, *J. Mater. Process. Technol.* 257 (2018) 227–233.
- [47] J. Archard, Contact and rubbing of flat surfaces, *J. Appl. Phys.* 24 (8) (1953) 981–988.
- [48] P.M. Sargent, Use of the Indentation Size Effect on Microhardness for Materials Characterization, *Microindentation Techniques in Materials Science and Engineering*, ASTM International, 1985.
- [49] M. Barnett, Twinning and the ductility of magnesium alloys: Part I: “Tension” twins, *Mater. Sci. Eng.: A* 464 (1–2) (2007) 1–7.

- [50] B. Mao, Y. Liao, B. Li, Gradient twinning microstructure generated by laser shock peening in an AZ31B magnesium alloy, *Appl. Surf. Sci.* 457 (2018) 342–351.
- [51] C.S. Roberts, *Magnesium and its Alloys*, Wiley, 1960.
- [52] S.-G. Hong, S.H. Park, C.S. Lee, Role of {10–12} twinning characteristics in the deformation behavior of a polycrystalline magnesium alloy, *Acta Mater.* 58 (18) (2010) 5873–5885.
- [53] B. Mao, Y. Liao, B. Li, Abnormal twin–twin interaction in an Mg–3Al–1Zn magnesium alloy processed by laser shock peening, *Scr. Mater.* 165 (2019) 89–93.
- [54] H. El Kadiri, J. Kapil, A. Oppedal, L. Hector Jr, S.R. Agnew, M. Cherkaoui, S. Vogel, The effect of twin–twin interactions on the nucleation and propagation of {101 2} twinning in magnesium, *Acta Mater.* 61 (10) (2013) 3549–3563.
- [55] J.J. Jonas, S. Mu, T. Al-Samman, G. Gottstein, L. Jiang, È. Martin, The role of strain accommodation during the variant selection of primary twins in magnesium, *Acta Mater.* 59 (5) (2011) 2046–2056.
- [56] B. Mao, B. Li, D. Lin, Y. Liao, Enhanced room temperature stretch formability of AZ31B magnesium alloy sheet by laser shock peening, *Mater. Sci. Eng.: A* 756 (2019) 219–225.
- [57] G. Nayyeri, W. Poole, C. Sinclair, S. Zaefner, Measurement of the critical resolved shear stress for basal slip in magnesium alloys using instrumented indentation, *Scr. Mater.* 156 (2018) 37–41.
- [58] M.A. Kumar, A. Kanjarla, S. Niezgodna, R. Lebensohn, C. Tomé, Numerical study of the stress state of a deformation twin in magnesium, *Acta Mater.* 84 (2015) 349–358.
- [59] C. Greiner, Z. Liu, R. Schneider, L. Pastewka, P. Gumbsch, The origin of surface microstructure evolution in sliding friction, *Scr. Mater.* 153 (2018) 63–67.
- [60] W. Zhang, J. Lu, W. Huo, Y. Zhang, Q. Wei, Microstructural evolution of AZ31 magnesium alloy subjected to sliding friction treatment, *Philos. Mag.* 98 (17) (2018) 1576–1593.
- [61] H. Abdolvand, M.R. Daymond, Internal strain and texture development during twinning: comparing neutron diffraction measurements with crystal plasticity finite-element approaches, *Acta Mater.* 60 (5) (2012) 2240–2248.
- [62] G. Gottstein, T. Al Samman, Texture development in pure Mg and Mg alloy AZ31, *Mater. Sci. Forum Trans. Technol. Publ.* (2005) 623–632.
- [63] P. Gao, S. Zhu, X. An, S. Xu, D. Ruan, C. Chen, H. Yan, S. Ringer, X. Liao, Effect of sample orientation and initial microstructures on the dynamic recrystallization of a magnesium alloy, *Mater. Sci. Eng.: A* 691 (2017) 150–154.
- [64] S. Mu, J.J. Jonas, G. Gottstein, Variant selection of primary, secondary and tertiary twins in a deformed Mg alloy, *Acta Mater.* 60 (5) (2012) 2043–2053.
- [65] D. Ando, J. Koike, Y. Sutou, Relationship between deformation twinning and surface step formation in AZ31 magnesium alloys, *Acta Mater.* 58 (13) (2010) 4316–4324.
- [66] W. Hutchinson, M. Barnett, Effective values of critical resolved shear stress for slip in polycrystalline magnesium and other hcp metals, *Scr. Mater.* 63 (7) (2010) 737–740.
- [67] Z. Wu, W. Curtin, The origins of high hardening and low ductility in magnesium, *Nature* 526 (7571) (2015) 62.
- [68] A. Oppedal, H. El Kadiri, C. Tomé, G. Kaschner, S.C. Vogel, J. Baird, M. Horstemeyer, Effect of dislocation transmutation on modeling hardening mechanisms by twinning in magnesium, *Int. J. Plast.* 30 (2012) 41–61.
- [69] S.H.C. Park, Y.S. Sato, H. Kokawa, Microstructural evolution and its effect on Hall–Petch relationship in friction stir welding of thixomolded Mg alloy AZ91D, *J. Mater. Sci.* 38 (21) (2003) 4379–4383.
- [70] T. Mukai, M. Yamanoi, H. Watanabe, K. Ishikawa, K. Higashi, Effect of grain refinement on tensile ductility in ZK60 magnesium alloy under dynamic loading, *Mater. Trans.* 42 (7) (2001) 1177–1181.